

The Ability of the CFD Approach to Investigate the Fluid and Wall Hemodynamics of Cerebral Stenosis and Aneurysm



Talaat Abdelhamid  and Ahmed G. Rahma 

1 Introduction

Investigation of hemodynamics characteristics in the vascular system of patients holds significant value for understanding and diagnosing various diseases [1, 2] such as stenosis [3], aneurysms of different types (saccular [4], fusiform [5], false, and dissection [6]), ..., etc. Each year, 15 million people worldwide experience a stroke, with 33.3% of them resulting in death and another 33.3% resulting in permanent disability. Although stroke is not a common occurrence among the young, it can occur due to high blood pressure when it does [7]. Currently, a major concern is gaining insight into cerebrovascular diseases and discovering the relationships they have with parameters of hemodynamics, such as the fluid vortex, and wall pressure/shear stress distribution. Luo et al. [8] conducted a computational fluid dynamics investigation on an MRI-based model of a cerebral artery with stenosis in order to examine its effect on the hemodynamics characteristics. The study began with a benchmark to ensure the boundary conditions and the computational methods, which were adopted by a straight pipe with an ideal symmetric stenosis of $d/D = 0.4$. Where the d/D , is the contraction diameter ratio to the pipe diameter. In the part two of the simulation. The simulations are done on MRI-based model of a cerebral

T. Abdelhamid (✉)

Physics and Mathematical Engineering Department, Faculty of Electronic Engineering, Menoufiya University, Menouf, Egypt

Shenzhen Institutes of Advanced Technology, Chinese Academy of Sciences, Shenzhen, China

e-mail: Talaat_abdelhamid@el-eng.menofia.edu.eg

A. G. Rahma

Physics and Mathematical Engineering Department, Faculty of Electronic Engineering, Menoufiya University, Menouf, Egypt

Department of Physics and Engineering, University of Strasbourg, Strasbourg, France

artery with 2 inlets and 15 outlets and measured boundary conditions such as the pressure outlet and the velocity inlet profiles are used. The results indicate that the stenosis is leading to a loss of pressure in the distal area.

Intracranial aneurysms are bulges in the intracranial arteries caused by a weakness in the blood vessel wall [9–11]. They affect a global population of between 0.5% and 6%. Unfortunately, rupture of these intracranial aneurysms (IAs) can occur in approximately 0.25% of cases, leading to death in 60% of cases [12, 13]. The study conducted by Souza et al. [14] aimed to analyze the impact of the hemodynamics and the structure on the behavior of intracranial aneurysms. By utilizing CFD simulations on a numerical model, they analyzed the parameters that have a significant effect on an aneurysm's rupture. The simulations were run at various Reynolds values (1–1000) using the Fluent 2020 R2 commercial package. The results revealed that an increase in Re leads to the formation of flow recirculation in the aneurysm. Additionally, the maximum values of WSS, displacement, and strain were observed at the highest Reynolds number.

Additionally, CFD simulations can be performed using two types of models [8, 15], the first is the benchmark model which is a simplified version of the vascular system [16–18]. The second is the patient-specific model, which is based on the real geometry of the patient's vasculature [19–21]. These simulations provide valuable information regarding the flow patterns and the wall stress/pressure distribution at cerebral vessels, which are crucial for understanding and diagnosing cerebrovascular diseases [22–24]. The results obtained from these simulations can be compared with the literature and validated to ensure the reliability of the CFD approach. Perinajová et al. [25] focused on analyzing the turbulence and WSS in the Narrowing of the aorta using computational fluid dynamics (CFD) simulations. To validate their findings, the researchers utilized a flow phantom of a vessel with 180 degree bending and narrowing with pulsating flow and compared the results with those obtained from a 4D-flow MRI technique. The results demonstrated a remarkable link between the experimental outcomes from the experimental approach and the CFD approach.

Xiang et al. [26] studied the effects of the hemodynamics on the rupture of IA. They found that the use of CFD simulations is effective in evaluating the risk of intracranial aneurysms when real patient data are available. The results indicated the importance of hemodynamic analysis in predicting the likelihood of an aneurysm rupture. Chen et al. [27] aimed to simplify the modeling process for studying the blood flow in a stroke patient's cerebral artery. Their research revealed that numerical simulations can be a time-efficient method for pre-and post-surgery planning, making it a valuable tool for medical professionals.

In this chapter, numerical simulations are performed for the entire cerebral arteries of two patients. The computational domain used for the simulation is divided into two segments (the benchmarks and the actual arteries reconstructed from the MRI). The problem is described, and the system of incompressible Navier-Stokes equations is introduced. Furthermore, a comprehensive study of the blood flow and wall hemodynamic parameters, including the WSS, wall pressure, and flow recirculation, is conducted on benchmarks before the solution is refined to incorporate actual patient-specific cerebral arteries.

2 Methodology

2.1 Problem Outline and the Numerical Approach

In this section, we examine two types of cerebral cardiovascular conditions – stenosis and aneurysm. The defined parameters of the simulation at the boundary conditions are derived from the ultrasonography scans. We employ a consistent CFD model to analyze the hemodynamics in both benchmark segment and patient-specific cerebral arteries segment with modified velocity/pressure profiles.

2.1.1 Cerebral Arteries Stenosis

In the first instance, the benchmark study involves simulating blood flow in pipes with a diameter of 3.5 mm and length of 61.6 mm, with a range of vascular Narrowing ratios variation from (0% to 60%) as depicted in Fig. 1. This contraction is assumed to represent an inborn medical condition in the patient. In the second case, a realistic scenario for MRI based model of the cerebral artery is taken into account [27], as shown in Fig. 16. Both studies are conducted using a consistent CFD model to present the blood flow dynamics in the given geometries.

2.1.2 Cerebral Arteries Aneurysm

The CFD simulations provide a comprehensive analysis for the flow characteristics of a benchmark of the intracranial artery (IA), as depicted in Fig. 2. The model is built and analyzed using boundary conditions derived from the literature [14]. Subsequently, the same characteristics are investigated for an MRI based model of

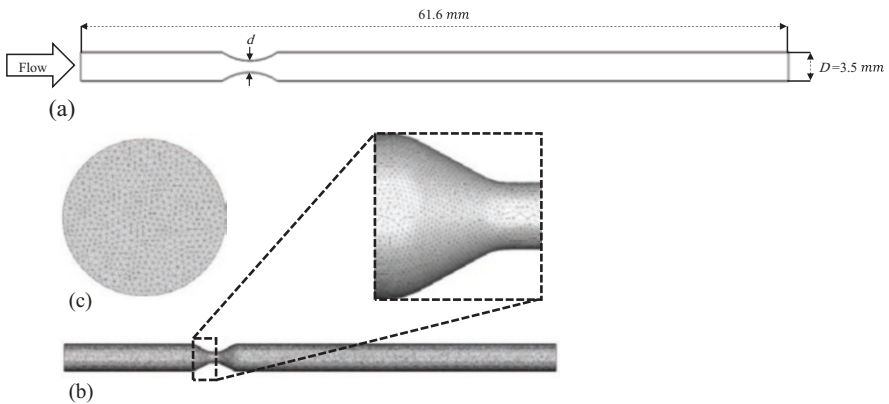


Fig. 1 (a) The benchmark domain of computation, (b) The model meshing and zoom in of the stenosis zone, and (c) zoom-in for the gridding system of the vessel inlet

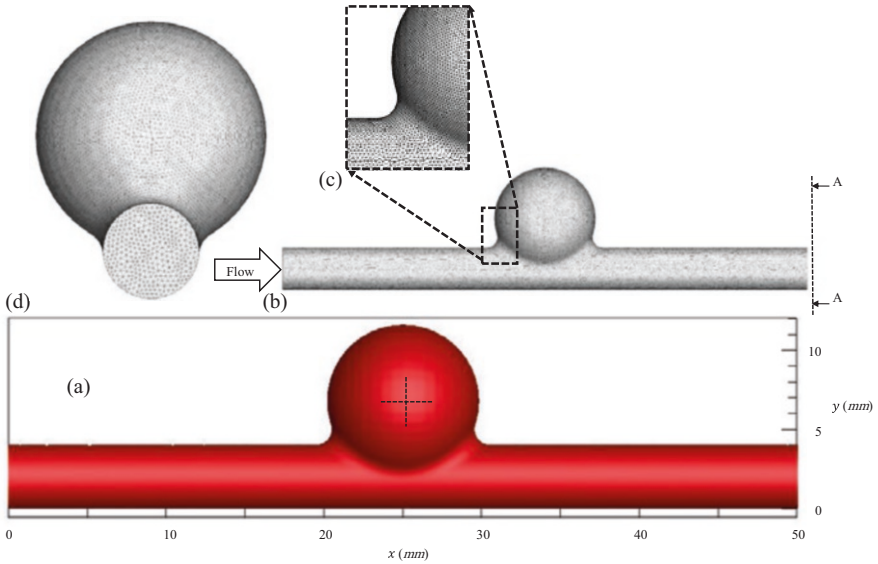


Fig. 2 (a) The computational domain (b) The meshing for the benchmark (c) Zoomed in for the meshing system of the aneurysm zone, and (d) Section A-A

a cerebral aneurysm at the anterior communicating artery (AAA). This model is built from MRI data by the commercial software package SimVascular (Fig. 17).

2.2 Governing Equations

Steady state, three-dimensional CFD simulations were conducted for both geometries. The flow of blood is governed by the differential equations presented in [28, 29]. The motion of blood was described using the Navier-Stokes equations in a laminar flow state, as follows:

$\Delta(\rho u) = 0$	(1)
	(2)
$\Delta(\rho u u) = -\frac{\partial p}{\partial x} + \Delta(\mu \nabla u)$	(3)
$\Delta(\rho u v) = -\frac{\partial p}{\partial y} + \Delta(\mu \nabla v)$	(4)
$\Delta(\rho u w) = -\frac{\partial p}{\partial z} + \Delta(\mu \nabla w)$	

Table 1 Properties of blood flow used for the benchmarks with stenosis

Properties	Value
Blood density	1063 (Kg.m ⁻³)
Velocity in	10.525 (cm/s)
Pressure at the inlet (Gauge)	11,999 Pa (90 mmHg)

Where “*u*”, “*v*”, and “*w*” are the blood *x*, *y*, *z* velocity components, respectively. The ρ parameter is representing the blood density while pressure defined as *P*. Blood is treated as an incompressible non-Newtonian fluid, with a viscosity model described by the Carreau model, and $\rho = 1063 \text{ kg/m}^3$. The walls of the computational domain are assumed to be rigid, with no slipping, as indicated in Tables 1, 2, and 3 for the blood properties at the stenosis, aneurysm and the four model parameter law (Carreau model) [14, 30]. The equations for the Carreau flow model can be found in [29].

$$\mu = H(t) \left(\mu_\infty + (\mu_0 - \mu_\infty) \left[1 + \gamma^2 \lambda^2 \right]^{\frac{n-1}{2}} \right) \tag{5}$$

Where (*H*(*t*)) represents the temperature dependence, which is described by the Arrhenius law.

$$H(t) = \exp \left[\alpha \left(\frac{1}{T - T_0} \right) - \left(\frac{1}{T_\alpha - T_0} \right) \right] \tag{6}$$

where α is the ratio of the activation energy to the thermodynamic constant and T_α is a reference temperature for which *H*(*t*) = 1. The T_0 is the temperature shift. The λ is the time constant.

Simulations were performed in two segments using the Ansys Fluent 19.2 software package [29] to solve the governing equations in a 3D computational domain. The Reynolds number was less than 2200, indicating laminar flow. Second-order upwind schemes were applied for all conservation equations. The pressure-velocity coupling used a coupled scheme and pressure was calculated with a second-order scheme. The pseudo transient for fluid and solid zones were 0.7 and 1.0, respectively, to achieve strong convergence for the complex blood flow.

2.3 Meshing

To ensure the accuracy of the results, a grid independence study was conducted and the resulting mesh can be seen in Figs. 1, 2, 16b, and 18e. The mesh was carefully constructed to be refined near the vessel wall and to maintain a *y* + value of

Table 2 Properties of blood flow used for the benchmarks with the aneurysm

Properties	Value (Unit)
Blood density	1063 (Kg.m ⁻³)
Velocity in	88.8 (cm/s)
Pressure at the inlet (Gauge)	0 (Pa Gauge)

Table 3 Carreau model four parameter values [30]

μ_{∞} (Pa. s)	μ_0	n	λ (s)
1.0	0.4360	0.360	3.30

approximately 1. Additionally, the standard wall treatment was employed to facilitate a smooth transition. As the CFD study of blood flow is strongly reliant on the wall effect, efforts were made to maintain a y^+ value close to 1, despite the laminar nature of the flow.

2.3.1 Cerebral Arteries Stenosis

The results of the computational fluid dynamics (CFD) simulations are presented by utilizing the tetrahedral mesh. The mesh size was established based on the recommendations of a previous study [8]. The total elements in the grid system are 897,865 for the benchmark with stenosis and 1,292,839 for the MRI-based model with stenosis. To ensure the accuracy of the results, a comprehensive mesh sensitivity study was imported from a previously study, which improved the confidence in the benchmark and the MRI-based model with stenosis models results [8].

2.3.2 Cerebral Arteries Aneurysm

For the IA benchmark, 522,323 tetrahedral elements are used. For the patient-specific IA, 722,724 tetrahedral elements are used to grid the realistic aneurysm model, for more details regarding the mesh size see [8].

2.4 Validation

2.4.1 The Benchmark with a Stenosis

The accuracy of the CFD results obtained in this study have been validated by comparing them with previously published results [8]. As seen in Fig. 3, the velocity and pressure contours produced by the present CFD model match well with those reported in [8]. Furthermore, a comparison of pressure drop values for the

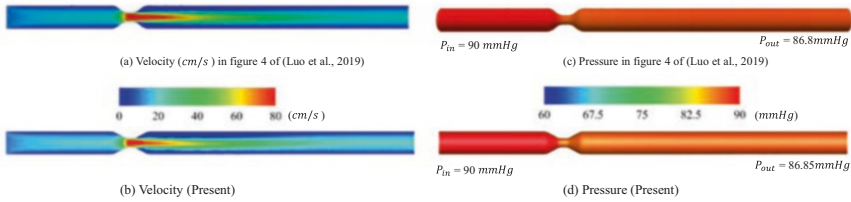


Fig. 3 The velocity and pressure contours for the benchmark with a 40% stenosis ($d/D = 0.4$) with velocity inlet 10.525 cm/s, for (a), (c) Luo et al. [8], and (b), (d) current study

benchmark between the present CFD results and those reported in [8] is shown in Table 4. The absolute error in the pressure drop between the current study and Luo, et al. [8] is found to be only 1.56%, which is considered to be acceptable. This validation confirms the validity of the CFD approach to investigate the hemodynamic of the blood.

2.4.2 The Benchmark with an Aneurysm

The CFD simulation outcomes were verified using data from previous studies [14]. The absolute error of the pressure drop across the (IA) benchmark was found to be around 3.261% according to Table 5 [14]. Additionally, Fig. 4 provides a visual representation of the results validation by comparing the wall pressure contours from the current study and the previous study in the literature review [14]. This comparison confirms the capability of the current CFD simulations to accurately evaluate the hemodynamic parameters, particularly for IA cases.

3 Results

3.1 Segment One, Results for the Benchmarks

3.1.1 The Benchmark with a Stenosis

This section presents the outcomes of the CFD simulation for the benchmark scenario involving the idealized straight vessel with a reduced area of flow. The impact of the contraction area ratio (d/D) on the artery inlet to outlet pressure ratio is depicted in Fig. 5. The results demonstrate that as the ratio increases, the pressure drop (pressure difference) across the artery contraction decreases, indicating a reduced energy loss for the flow passing through the contraction.

A. The pressure distribution:

Figure 6 illustrates the pressure contour across the benchmarks with stenosis. The pressure drop increases with decreasing the d/D ratio. This denotes that as the

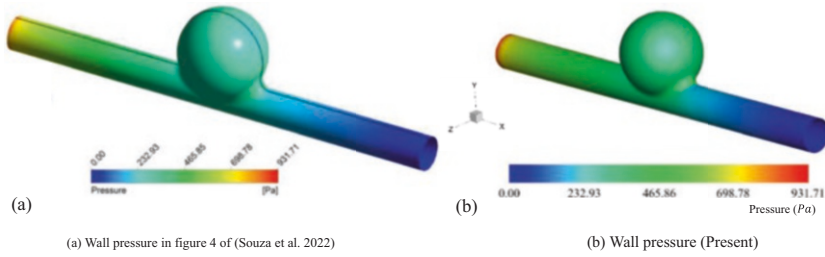


Fig. 4 The wall pressure distribution across the benchmark of an aneurysms where the inlet velocity = 88.8 cm/s, for **(a)** MacDonald et al. [14], and **(b)** present study

Table 4 The pressure drops for the benchmark with a stenosis $d/D = 0.4$, compared with the literature results

Reference	$P_{in} - P_{out}$
Luo et al. [8]	3.200 (mmHg)
Present study	3.150 (mmHg)
Absolute error	1.563 (%)

Table 5 The pressure drop across the benchmark with an aneurysm, compared with the literature results

Reference	$P_{in} - P_{out}$
Souza et al. (2022) [14]	726.1200 (Pa)
Present study	749.8021 (Pa)
Absolute error	3.26 (%)

cross-section area of the contraction decreases, the required energy to overcome the losses also increases. The results of the pressure difference can be seen in Fig. 5, which shows the inlet and outlet pressure ratio with the contraction area ratio. The development of the flow in the benchmark can be observed in Fig. 6g. The pressure profile along the centerline of the model demonstrates that the flow has reached a fully developed state, and the entrance length is adequate to achieve this. The error was found to be 2.1%, which is considered acceptable within computational standards. Reducing the area of the vessel can result in an increase in the blood velocity and the formation of vortices as in Figs. 7, 8, and 9. These changes in hemodynamics can greatly affect the flow dynamics.

B. The flow structures

The contraction of the blood flow leads to the formation of eddies and vortices, which are particularly evident at lower area ratios. This flow behavior is a result of the contraction or expansion of the blood flow and can extract energy from the flow and even impede its passage in some cases. A lower area of contraction leads to

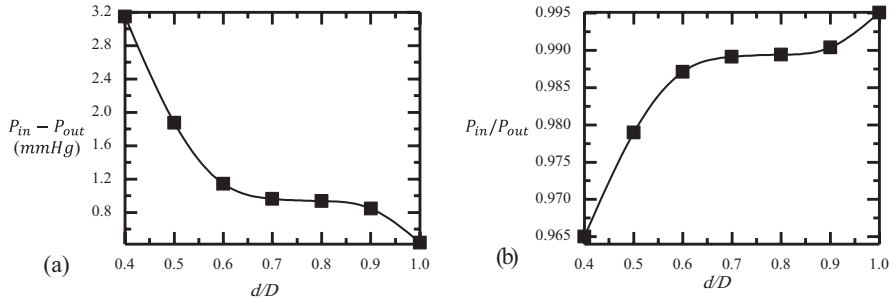


Fig. 5 The artery from inlet to outlet (a) The pressure drop, and (b) Pressure ratio of the benchmarks with stenosis

blood flow accumulation, which is indicative of a medical issue and may necessitate a therapeutic intervention. These flow characteristics can be easily visualized in the streamline plots presented in Figs. 8 and 9. Additionally, the alteration of the blood flow hemodynamics is further demonstrated by the increase in blood velocity and the creation of vortices, as shown in Figs. 7, 8, and 9. The formation of vortices, due to an increase in fluid flow turbulence, causes asymmetry in the flow and is evident in values of d/D such as 0.4, 0.5, and 0.6, as depicted in Figs. 7a–c and 8a–c.

C. The wall shear stress (WSS):

The relationship between the stenosis geometry and the wall shear stress (WSS) is illustrated in Fig. 10. The WSS value at the stenosis zone increases as the area of the stenosis (d/D) decreases. However, beyond the stenosis zone, the WSS value begins to decline as the d/D value decreases. This decline in WSS value can result in the formation of flow recirculation, particularly when d/D is less than or equal to 0.4, as demonstrated in Figs. 9 and 10h.

3.1.2 The Benchmark with an Aneurysm

This section presents a thorough examination of the blood flow characteristics, including the wall pressure/shear stress, and recirculation flow within the IA benchmark.

A. The pressure distributions

In Figs. 4 and 11, a decrease in wall pressure is observed in the direction of the flow, with an exception for the ideal IA zone. In this zone, the wall pressure remains constant due to the presence of recirculation flow. In the region near the trailing edge of the intracranial aneurysm, the flow direction is observed to reverse due to the interaction between the wall and the flow. This interaction results in an increase in wall pressure values.

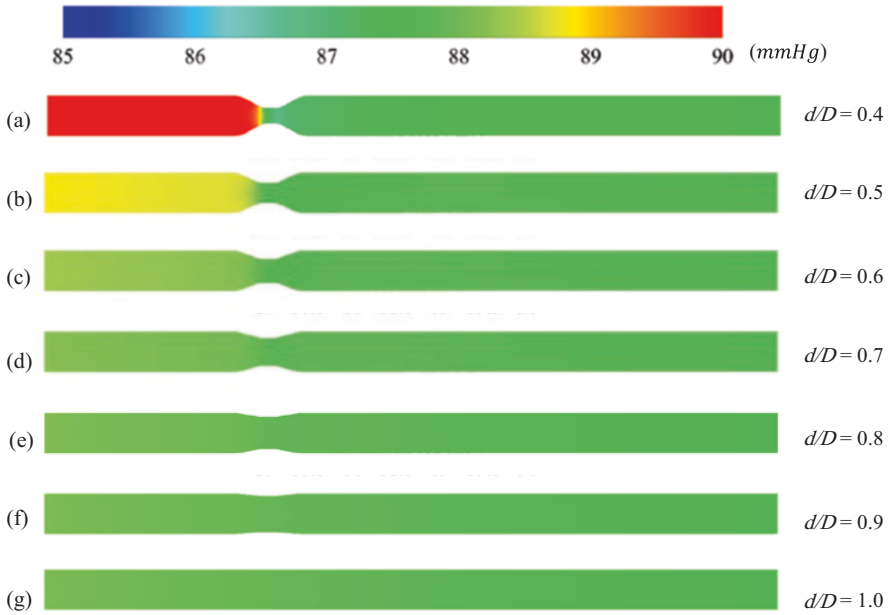


Fig. 6 Pressure distribution contours at center cross section for the benchmark with different d/D ratio

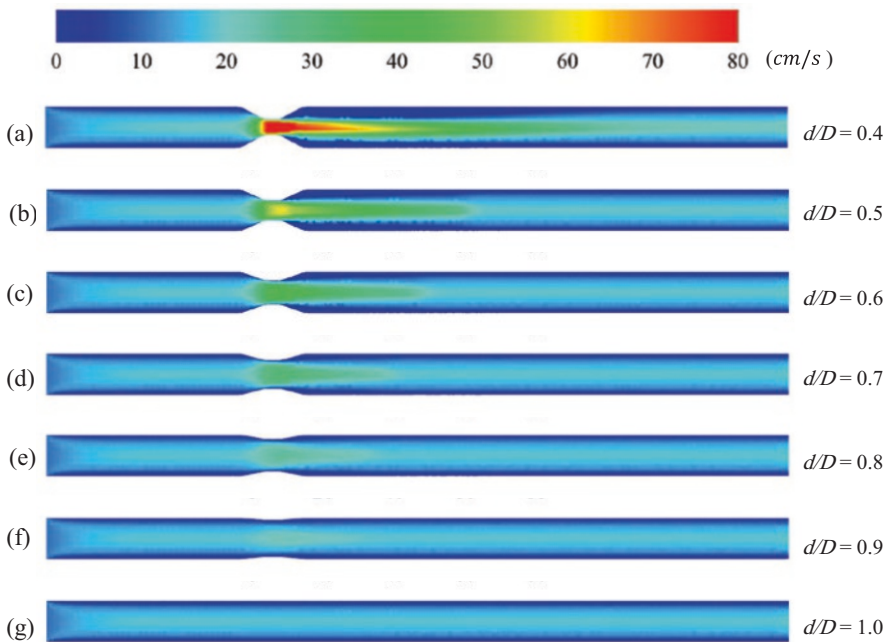


Fig. 7 Velocity distribution contours at center cross section for the benchmark with different d/D

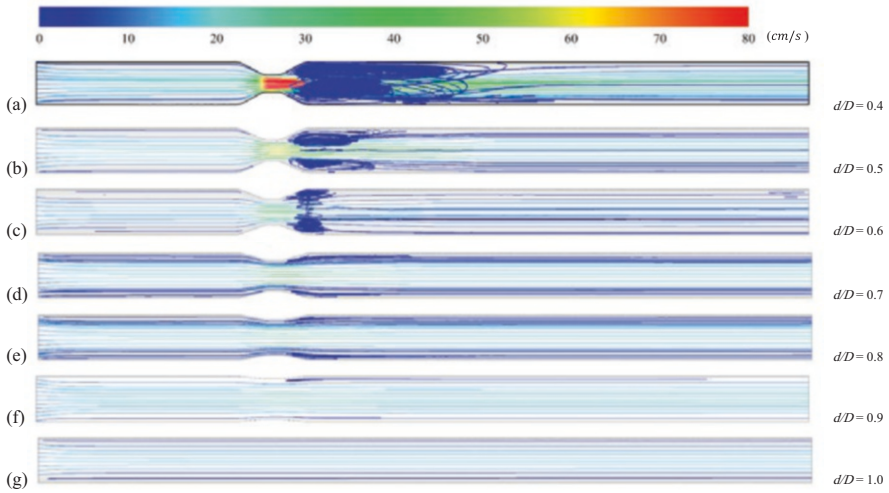


Fig. 8 The velocity streamline contours for the benchmark with different d/D

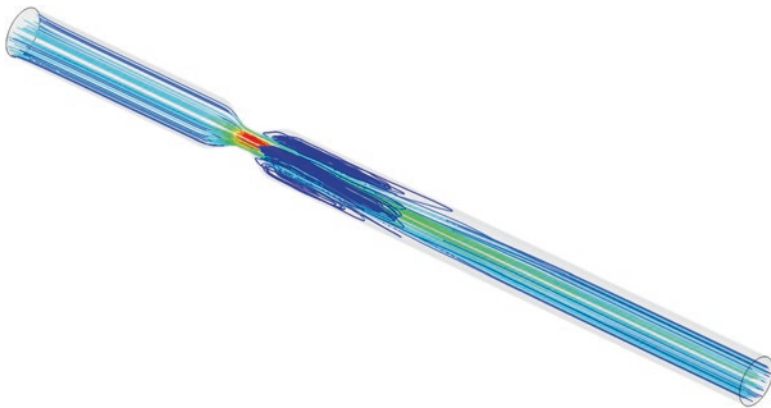


Fig. 9 Three dimensional velocity streamlines contours for the benchmark at $d/D = 0.4$

B. The flow structure:

The blood velocity has a profound influence on the occurrence of the flow recirculation. As the velocity distribution increases, the likelihood of flow recirculation also increases [14, 31]. This can be seen in Fig. 12 where two flow regimes are present. The flow regime is seen near the inlet and the outlet of the benchmark, while the formation of vortices is seen close to and inside the dilation. The recirculation of the flow in the aneurysm zone is a result of using a high flow velocity (88.8 cm/s), which leads to separation at the trailing edge of the IA and the formation of the flow recirculation.

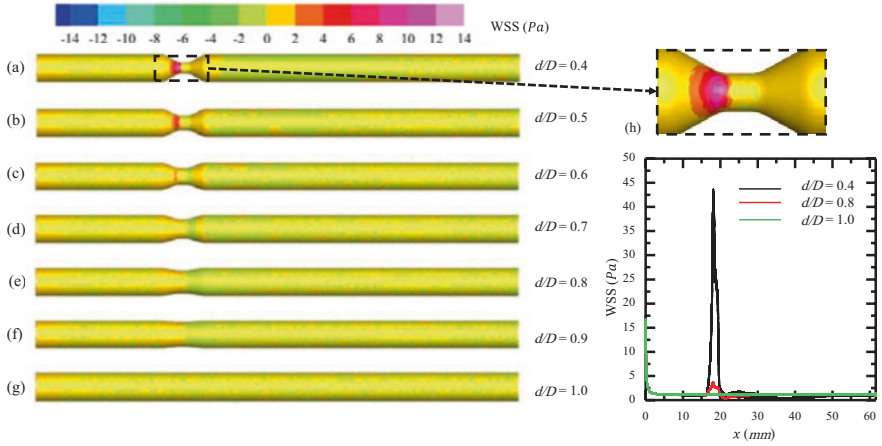


Fig. 10 The WSS distribution contours for the benchmark with variable d/D , and (h) Zoomed-in view for the stenosis zone at $d/D = 0.4$

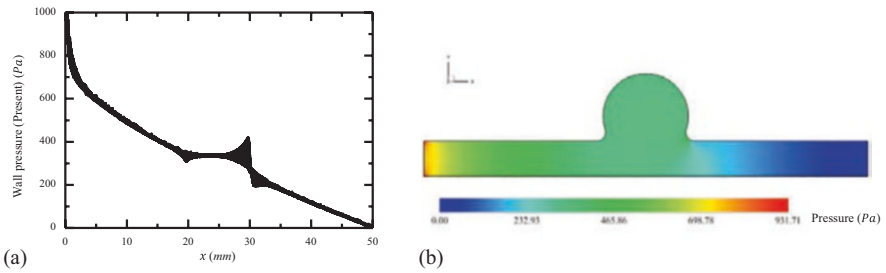


Fig. 11 The magnitude of the wall pressure (a) along x axis and (b) xy cross-section contour of pressure

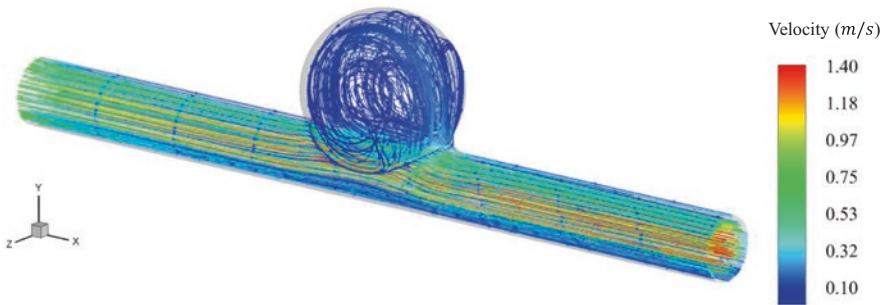


Fig. 12 Three-dimensional velocity streamlines contours for the intracranial aneurysm benchmark

The velocity profile at different locations is shown in Fig. 13. Three different cuts along the x direction are taken to display the velocity contours at three different positions – inlet, outlet, and the aneurysm center. The velocity profiles at the inlet and the outlet exhibit a symmetric distribution around the center of the y axis. The flow at the inlet is fully developed and follows a plug velocity boundary condition. The flow at the outlet is also fully developed. However, the presence of the saccular aneurysm results in a change in the velocity profile’s symmetry. The right side of the aneurysm velocity profile exhibits a higher decrease in velocity compared to the center of the cylinder.

C. The wall shear stress

In Fig. 14, the configuration of the WSS around the dilation is analyzed. The behavior of the wall shear stress is consistent with the wall pressure configuration displayed in Figs. 4 and 11. The WSS decreases along the flow direction, except around the bulge. The WSS at the start of the aneurysm region stays unchanged because of the existence of flow recirculation. Interaction and separation at the rear edge of the bulge causes an increase in the WSS at its outlet.

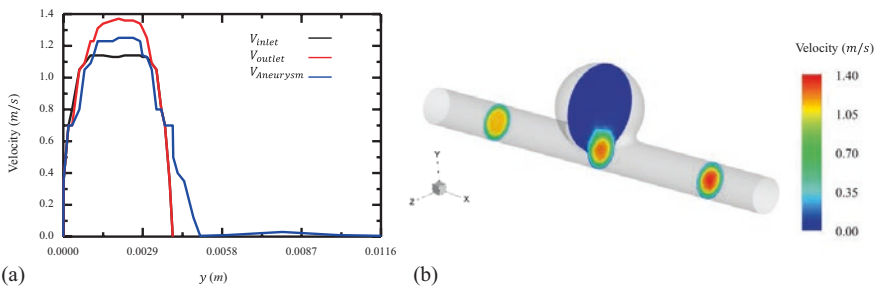


Fig. 13 (a) Absolute velocity curves at three different positions (b) three cross-sections in the benchmarks corresponding to the plots at (a), respectively

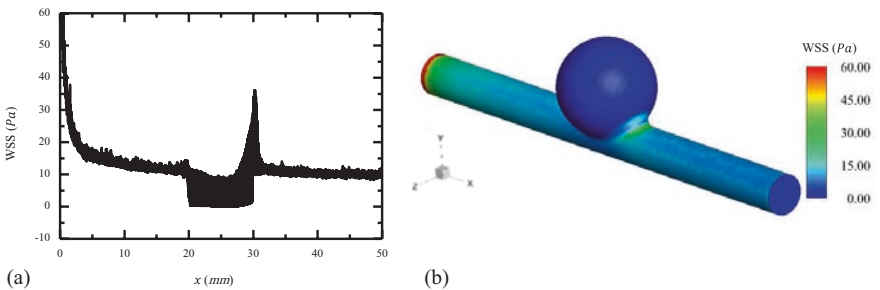


Fig. 14 (a) The magnitude of the WSS along the x direction, and (b) the magnitude of the WSS contour along the benchmark with intracranial aneurysm, respectively

3.2 Segment Two, Results for MRI-Based Models of the Cerebral Arteritis

In this section, CFD simulations were performed on realistic models of a stenosis and aneurysm in a patient-specific cerebral artery, reconstructed from MRI data. The computational domains were created using the SimVascular software as outlined in the methodology. An actual MRI of a cerebral artery was utilized, with a stenosis presented in the artery left middle part of the artery as shown in Fig. 15. The stenosis exhibits a contraction of approximately 55%, the model involved 2 inlets and 35 outlets (Fig. 16).

Regarding the aneurysm, the dimensions of the yz , xy , and xz planes are 9.91 mm , 6.62 mm , and 8.082 mm , respectively. We observe a significant increase of about 200% in the yz plane compared to the main vessel branch, Figs. 17 and 18.

Additionally, the velocity profiles at the artery inlet and the pressure profiles at the artery outlet that were both computed and measured are displayed in Fig. 19. The measured velocity profiles at the inlet and the pressure profiles at the outlet obtained through ultrasonography are shown over 4 cycles in Fig. 19a, c, respectively. The computed velocity profiles at the artery inlet and the pressure profiles at the artery outlet for one cycle, represented by red lines, are shown in Fig. 19b, d, respectively. These were extracted using polynomials equations obtained through curve fitting.

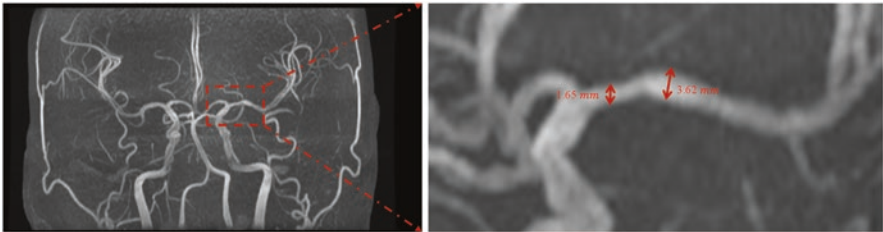


Fig. 15 MRI of the patient cerebral arteries with 55% area reduction stenosis [27]

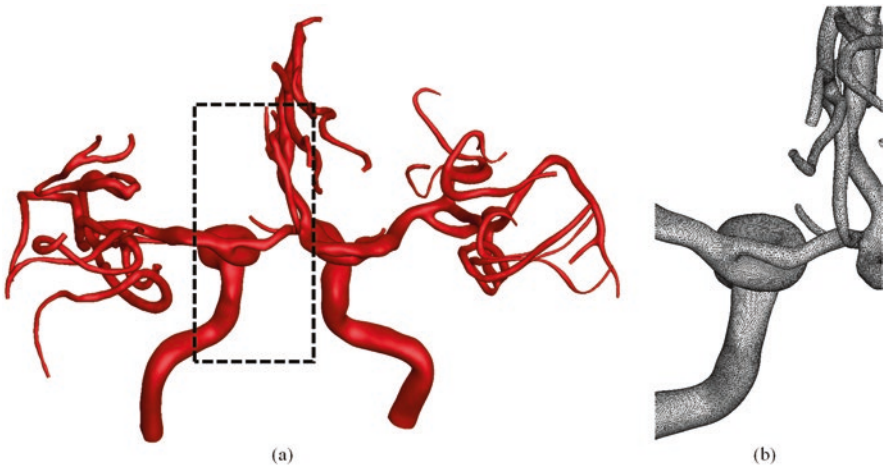


Fig. 16 (a) The MRI- based computational domain, and (b) a zoomed-in view of meshing system

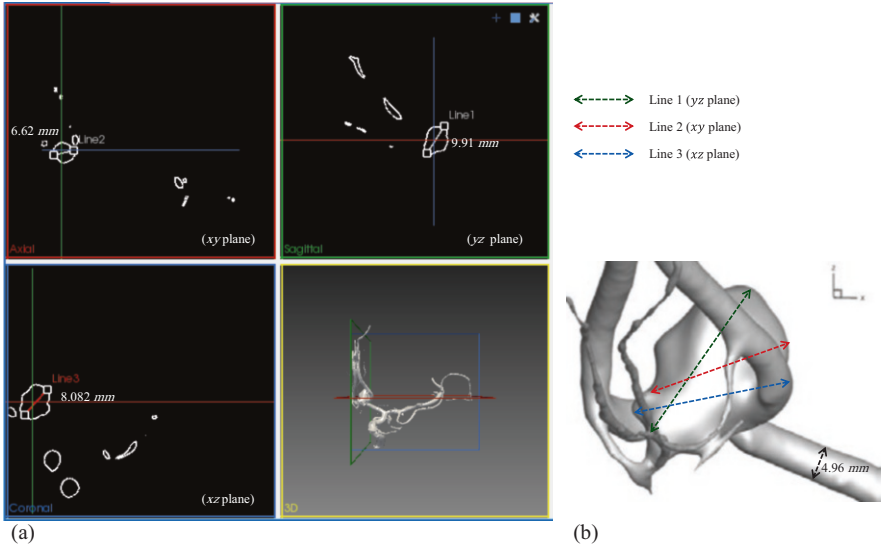


Fig. 17 (a) The aneurysm dimensions in the (yz, xy, and xz) directions, and (b) the dimension of the vessel before the aneurysm inlet

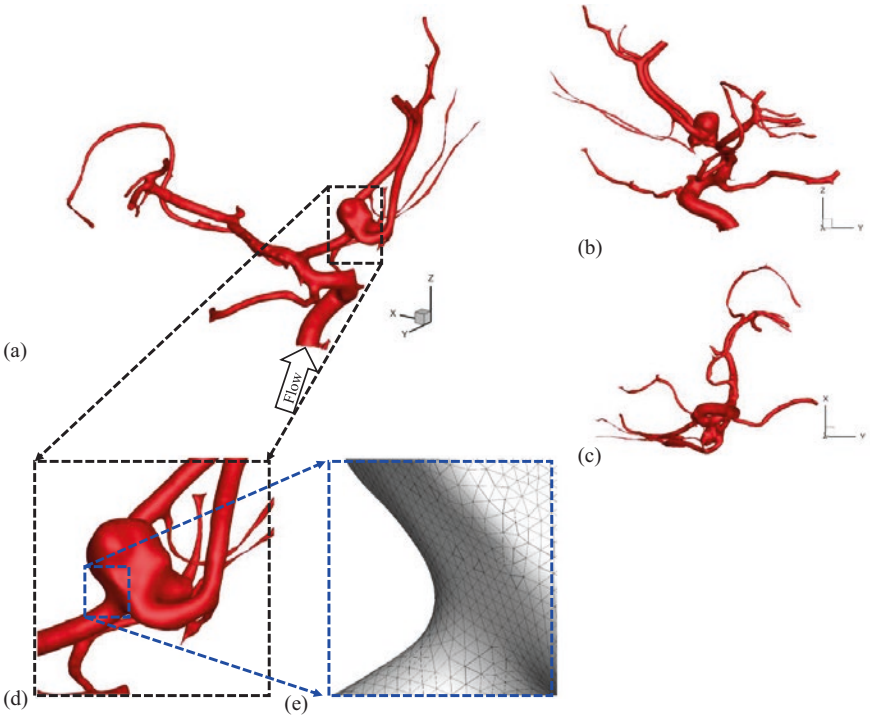


Fig. 18 (a) The MRI-based IA computational domain, (b, c) side-views of the model at yz, xy planes, respectively, (d) Zoomed in view of the IA aneurysm, and (e) zoomed-in view of the meshing system

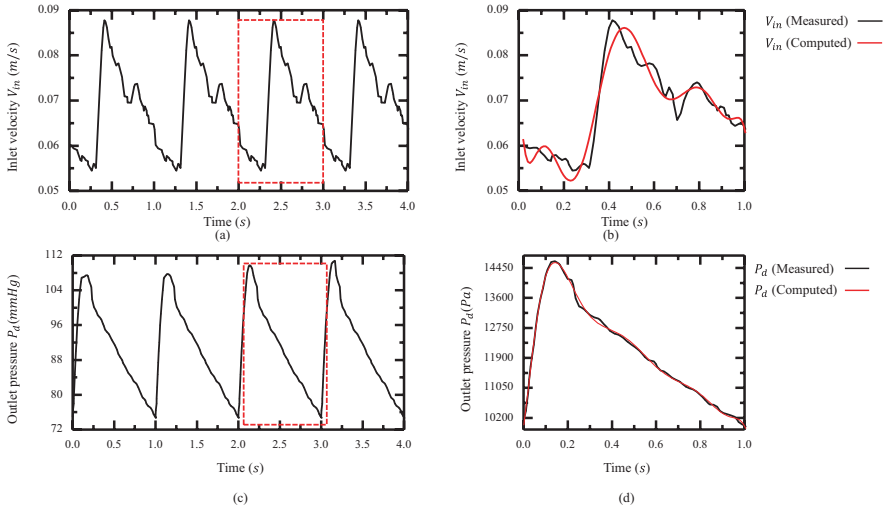


Fig. 19 (a–b) The cerebral artery inlet velocity profiles, and (b–c) the cerebral artery outlet pressure (c) in *mmHg*, and (d) *Pa*

3.2.1 MRI-Based Model With Stenosis

A. The flow structure:

1. Figure 20 displays the velocity streamlines and contours distribution. The velocity streamlines are displayed with a range from 0 to 0.7 meters per second. The zoomed-in views support the predictions made based on the results from segment one, as shown in Figs. 8 and 9. The formation of blood eddies and vortices can be seen as a result of the reduced area of the artery, causing a change in the symmetrical blood flow distribution near the wall. In Fig. 21, the velocity at the stenosis area and in the middle of the artery is higher compared to that near the vessel wall. The velocity configuration is not symmetrical, as seen in the zoomed-in view of the stenosis artery, when compared to the section of the normal artery without stenosis.

B. Wall hemodynamics:

2. In Fig. 20b, the pressure is seen to vary from 74 to 80 *mmHg*, and as anticipated from the benchmark results, the pressure drop is observed to increase between the inlet and outlet of the constricted area at the stenosis. Figure 22 shows that the WSS in the vicinity of the stenosis is more significant than that at other regions. A decrease in the WSS after the stenosis region is also observed in MRI-based model. High wall shear stress in the stenosis zone could produce an embolism due to the fluid-thrombus interaction, leading to vessel blockage and stroke.

3.2.2 MRI-Based Model with Aneurysm

A. The flow structure:

In Fig. 23a, b, the formation of vortex at the anterior communicating artery aneurysm (AAA) greatly impacts the wall pressure/shear stress and flow regimes at the outlet. The interaction of the fluid with the dilation wall results in flow separation.

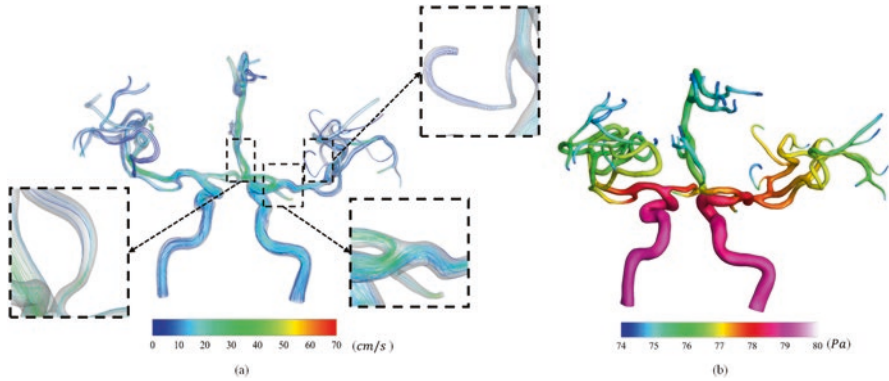


Fig. 20 (a) The velocity streamlines contours and (b) wall-pressure contour for the MRI-based model

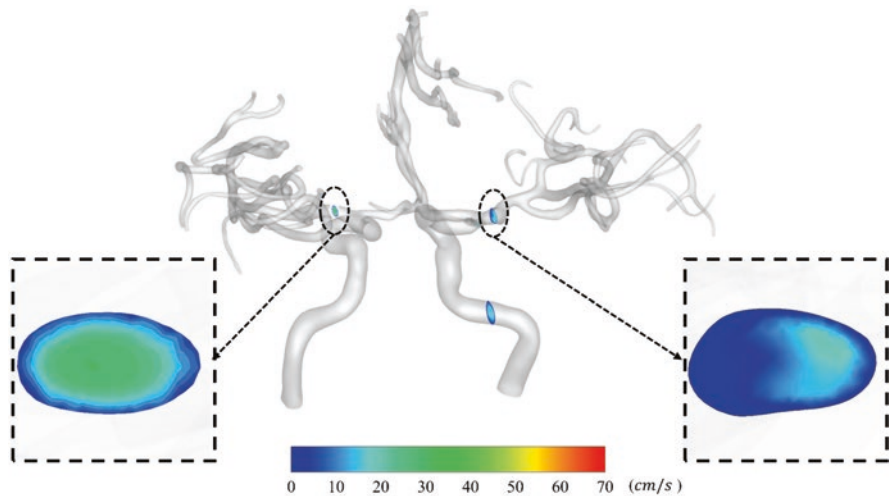


Fig. 21 Two cross-section views of velocity contours for the MRI-based model

The zone of separation experiences the highest values of both wall pressure and wall shear stress.

The velocity contours of the IA zone is displayed in two cross-sections, one in the yz plane and one in the xz plane, as shown in Fig. 24. In the yz plane, the highest velocity value is seen at the inlet of the artery and gradually decreases in the z direction, with the exception of the flow recirculation area. The interaction between the fluid and the dilation wall is depicted in Fig. 24c, as the velocity distribution vector shows the reverse flow which is responsible for flow recirculation in the z direction. In the xz plane, the highest magnitude of velocity is seen at the core of the flow inlet and decreases gradually in the z direction, except for the values close to the wall in

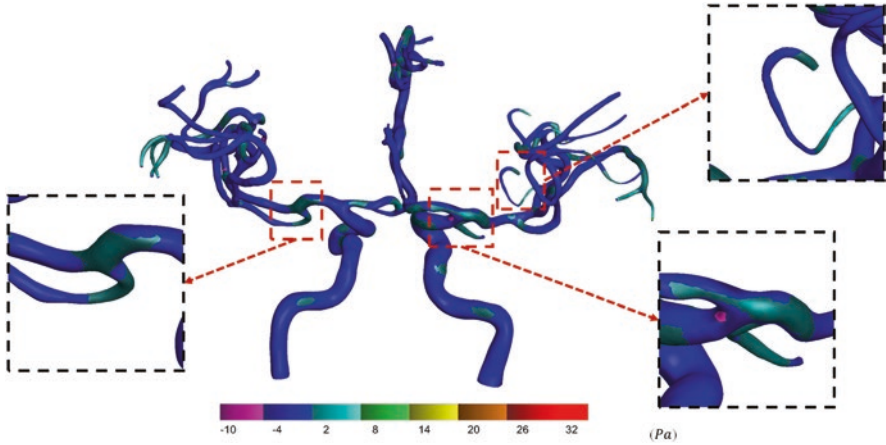


Fig. 22 The wall shear stress contour and zoom-in views of the areas close to the stenosis, and the branching for the MRI-based model

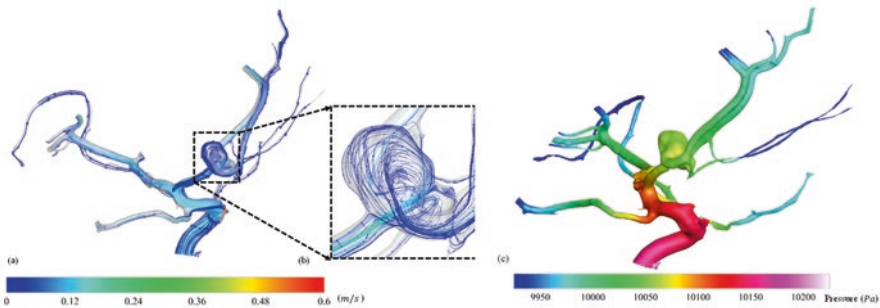


Fig. 23 (a) The velocity streamlines for the AAA (b) Zoomed-in view of the IA, and (c) the wall pressure contour along the MRI-based model of the IA

the x direction. The velocity is greater next to the wall in the right part of the x direction, due to the presence of the recirculation flow near the flow-wall interaction zone, as demonstrated in Fig. 24b and d.

B. Wall Hemodynamics:

The examination of the wall characteristics like the WSS and the wall pressure is crucial in comprehending the behavior of aneurysm. Figures 25 and 23c, the blood flow patterns impact the hemodynamics wall parameters. The wall shear stress and the wall pressure exhibit a gradual decline as the blood flows through, with the exception of the aneurysm area which is depicted in the benchmark at segment one (Figs. 11 and 14). In Fig. 25b, c, the wall shear stress near the inlet of the dilation is higher compared to the outlet zone. The fluid interaction with the edges results in an increase in the WSS at the outlet edges. The changes in WSS help predict the likelihood of aneurysm rupture, as research indicates that ruptures tend to occur in regions with low wall shear stress [32].

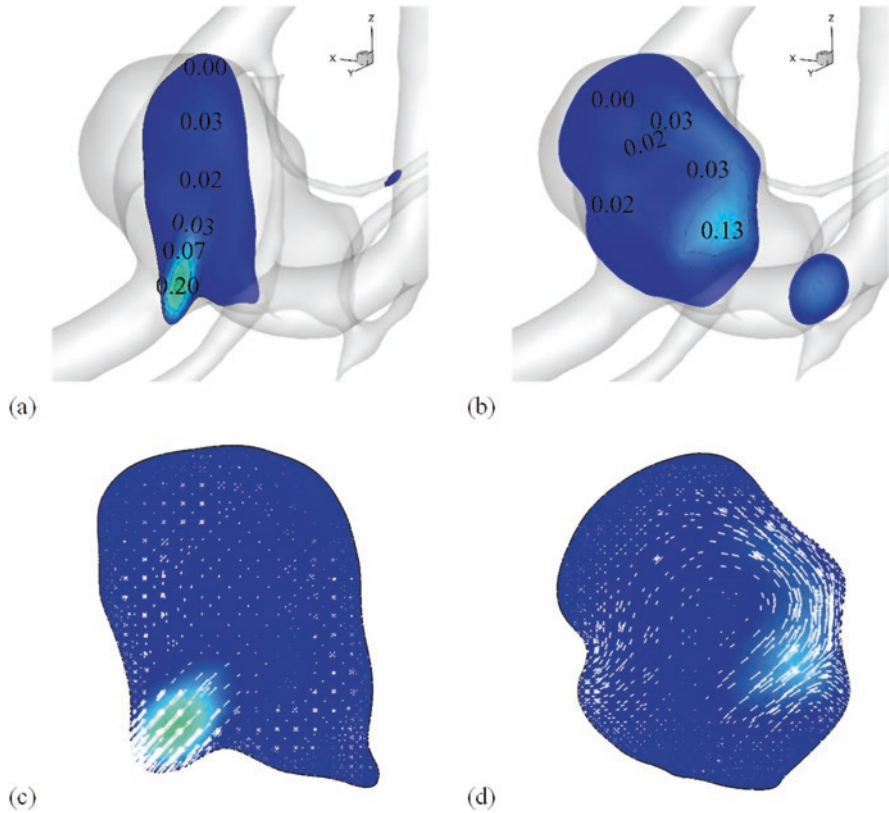


Fig. 24 Cross-sections of velocity distribution at (a–b) yz-plane and xz- plane, respectively. Cross-section of the velocity vector at (c–d) yz plane and xz plane, respectively

4 Conclusion

In this chapter, a systematic image-based computational fluid dynamics (CFD) method was introduced to simulate the blood flow in both benchmark and MRI-based models, to understand the hemodynamics of the complex vascular system. The results showed that the pressure difference across the arterial stenosis was reduced with increasing area ratio (d/D), resulting in less flow energy loss. The stenosis lead to increasing the velocity of the blood and produce vortexes, in some cases leading to vessel occlusion. The velocity at the stenosis areas was found to be relatively high and unevenly distributed, with high wall shear stress (WSS) values near the contraction area which could increase the risk of embolism and vessel occlusion. The presence of the saccular aneurysms in the vascular system revealed recirculation flow and uneven variation in WSS that may indicate the location of rupture. The wall pressure and the WSS behavior were found to be qualitatively matching.

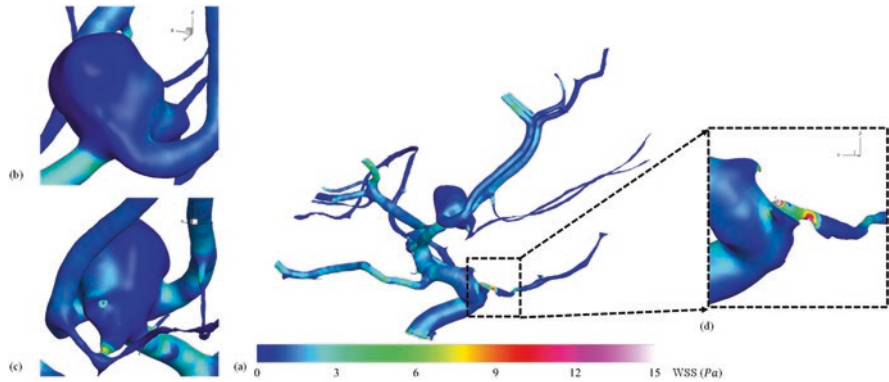


Fig. 25 (a) The WSS contour along the MRI-based model of the intracranial aneurysm. Zoom in view of (b) the inlet of the aneurysm inlet, (c) the outlet of the aneurysm, and (d) the stenosis zone

Acknowledgment This work was partially supported by the Science and Technology Development Fund (STDF) of Egypt, project No: 39385.

Availability of Data The data that support the findings of this study are available from the corresponding author upon reasonable request.

Conflict of Interest The authors declare that they have no conflict of interest.

References

3. Nixon, A. M., Gunel, M., & Sumpio, B. E. (2010). The critical role of hemodynamics in the development of cerebral vascular disease. *Journal of Neurosurgery*, *112*, 1240–1253.
4. Cecchi, E., Giglioli, C., Valente, S., Lazzeri, C., Gensini, G. F., Abbate, R., & Mannini, L. (2011). Role of hemodynamic shear stress in cardiovascular disease. *Atherosclerosis*, *214*, 249–256.
5. Rahma, A. G., Yousef, K., & Abdelhamid, T. (2022). Blood flow CFD simulation on a cerebral artery of a stroke patient *SN Applied Sciences*, *4*, 261.
6. Rahma, A. G., & Abdelhamid, T. (2023). Hemodynamic and fluid flow analysis of a cerebral aneurysm: A CFD simulation *SN Applied Sciences*, *5*, 62.
7. Elhanafy, A., Guaily, A., & Elsaid, A. (2019). Numerical simulation of Oldroyd-B fluid with application to hemodynamics. *Advances in Mechanical Engineering*, *11*, 1–7.
8. Karmonik, C., Yen, C., Grossman, R. G., Klucznik, R., & Benndorf, G. (2009). Intra-aneurysmal flow patterns and wall shear stresses calculated with computational flow dynamics in an anterior communicating artery aneurysm depend on knowledge of patient-specific inflow rates. *Acta Neurochirurgica*, *151*, 479–485.
9. Department of Health Statistics and Informatics. (2021). World Health Organization Geneva. Health topics. Stroke, Cerebrovascular accident.
10. Luo, L., Shiu, W. S., Chen, R., & Cai, X. C. (2019). A nonlinear elimination preconditioned inexact Newton method for blood flow problems in human artery with stenosis. *Journal of Computational Physics*, *399*, 108926.

11. Thompson, B. G., Brown, R. D., Amin-hanjani, S., Broderick, J. P., Cockcroft, K. M., Connolly, E. S., Duckwiler, G. R., Harris, C. C., Howard, V. J., Johnston, S. C. C., Meyers, P. M., Molyneux, A., & Ogilvy, C. S. (2015). AHA/ASA Guideline Guidelines for the Management of Patients with Unruptured Intracranial Aneurysms. *Stroke*, *46*(8), 2368–2400.
12. Schievink, W. I. (1997). Intracranial aneurysms. *The New England Journal of Medicine*, *336*, 28–40.
13. Johnston, S. C., Higashida, R. T., Barrow, D. L., Caplan, L. R., Dion, J. E., Hademenos, G., Hopkins, L. N., Molyneux, A., Rosenwasser, R. H., Vinuela, F., & Wilson, C. B. (2002). Recommendations for the endovascular treatment of intracranial aneurysms a statement for healthcare professionals from the committee on cerebrovascular imaging of the american heart association council on cardiovascular radiology. *Stroke*, *33*, 2536–2544.
14. Amenta, P. S., Yadla, S., Campbell, P. G., Maltenfort, M. G., Dey, S., Ghosh, S., Ali, M. S., Jallo, J. I., Tjounmakaris, S. I., Gonzalez, L. F., Dumont, A. S., Rosenwasser, R. H., & Jabbour, P. M. (2012). Analysis of nonmodifiable risk factors for intracranial aneurysm rupture in a large, retrospective cohort. *Neurosurgery*, *70*, 693–701.
15. MacDonald, D. E., Najafi, M., Temor, L., & Steinman, D. A. (2022). Spectral Bandedness in high-Fidelity computational fluid dynamics predicts rupture status in intracranial aneurysms. *Journal of Biomechanical Engineering*, *144*, 061004.
16. Souza, M. S., Souza, A., Carvalho, V., Teixeira, S., Fernandes, C. S., Lima, R., & Ribeiro, J. (2022). Fluid flow and structural numerical analysis of a cerebral aneurysm model. *Fluids*, *7*, 100.
17. Nordgaard, H., Swillens, A., Nordhaug, D., Kirkeby-Garstad, I., Van Loo, D., Vitale, N., Segers, P., Haaverstad, R., & Lovstakken, L. (2010). Impact of competitive flow on wall shear stress in coronary surgery: Computational fluid dynamics of a LIMA-LAD model. *Cardiovascular Research*, *88*, 512–519.
18. Lin, K. Y., Shih, T. C., Chou, S. H., Chen, Z. Y., Hsu, C. H., & Ho, C. Y. (2016). Computational fluid dynamics with application of different theoretical flow models for the evaluation of coronary artery stenosis on CT angiography: Comparison with invasive fractional flow reserve. *Biomedical Physics and Engineering Express*, *2*, 1–11.
19. Shanmugavelayudam, S. K., Rubenstein, D. A., & Yin, W. (2010). Effect of geometrical assumptions on numerical modeling of coronary blood flow under normal and disease conditions. *Journal of Biomechanical Engineering*, *132*, 61004.
20. Katritsis, D., Kaiktsis, L., Chaniotis, A., Pantos, J., Efstathopoulos, E. P., & Marmarelis, V. (2007). Wall shear stress: Theoretical considerations and methods of measurement. *Progress in Cardiovascular Diseases*, *49*, 307–329.
21. Murayama, Y., Fujimura, S., Suzuki, T., & Takao, H. (2019). Computational fluid dynamics as a risk assessment tool for aneurysm rupture. *Neurosurgical Focus*, *47*, E12.
22. Morris, P. D., Narracott, A., Von Tengg-Kobligh, H., Soto, D. A. S., Hsiao, S., Lungu, A., Evans, P., Bressloff, N. W., Lawford, P. V., Rodney Hose, D., & Gunn, J. P. (2016). Computational fluid dynamics modelling in cardiovascular medicine. *Heart*, *102*, 18–28.
23. Wellnhofer, E., Osman, J., Kertzsch, U., Affeld, K., Fleck, E., & Goubergrits, L. (2010). Flow simulation studies in coronary arteries—Impact of side-branches. *Atherosclerosis*, *213*, 475–481.
24. Boutsianis, E., Guala, M., Olgac, U., Wildermuth, S., Hoyer, K., Ventikos, Y., & Poulikakos, D. (2009). CFD and PTV steady flow investigation in an anatomically accurate abdominal aortic aneurysm. *Journal of Biomechanical Engineering*, *131*, 1–15.
25. Ford, M. D., Nikolov, H. N., Milner, J. S., Lownie, S. P., DeMont, E. M., Kalata, W., Loth, F., Holdsworth, D. W., & Steinman, D. A. (2008). PIV-measured versus CFD-predicted flow dynamics in anatomically realistic cerebral aneurysm models. *Journal of Biomechanical Engineering*, *130*, 1–9.

26. Hoi, Y., Woodward, S. H., Kim, M., Taulbee, D. B., & Meng, H. (2006). Validation of CFD simulations of cerebral aneurysms with implication of geometric variations. *Journal of Biomechanical Engineering*, *128*, 844–851.
27. Perinajová, R., Juffermans, J. F., Mercado, J. L., Aben, J. P., Ledoux, L., Westenberg, J. J. M., Lamb, H. J., & Kenjereš, S. (2021). Assessment of turbulent blood flow and wall shear stress in aortic coarctation using image-based simulations. *Biomedical Engineering Online*, *20*, 1–21.
28. Xiang, J., Tutino, V. M., Snyder, K. V., & Meng, H. (2014). CFD: Computational fluid dynamics or confounding factor dissemination? The role of hemodynamics in intracranial aneurysm rupture risk assessment. *American Journal of Neuroradiology*, *35*, 1849–1857.
29. Chen, R., Wu, B., Cheng, Z., Shiu, W. S., Liu, J., Liu, L., Wang, Y., Wang, X., & Cai, X. C. (2020). A parallel non-nested two-level domain decomposition method for simulating blood flows in cerebral artery of stroke patient. *International Journal for Numerical Methods in Biomedical Engineering*, *36*, 1–20.
30. Versteeg, H. K. (1955). *An introduction to computational fluid dynamics: The finite volume method*. Longman Scientific & Technical/Wiley.
31. Fluent, A. (2013). *Ansys fluent theory guide*. ANSYS Inc., USA 15317 724–746
32. Zouggari, L. (2018). The role of biomechanics in the assessment of carotid atherosclerosis severity: A numerical approach OPEN ACCESS *World. Journal of Vascular Surgery*, *1*, 1007.
33. Usmani, A. Y., & Patel, S. (2018). Hemodynamics of a cerebral aneurysm under rest and exercise conditions. *International Journal of Energy for a Clean Environment*, *19*, 119–136.
34. Yoshiki, K., Misaki, K., Nambu, I., Fukui, I., Mohri, M., Uchiyama, N., & Nakada, M. (2017). Intraoperative rupture of unruptured cerebral aneurysm during craniotomy: A case report. *Case Reports in Neurology*, *9*, 261–266.